sensors

MDPI

Article

Micromachined Vibrating Ring Gyroscope Architecture with High-Linearity, Low Quadrature Error and Improved Mode Ordering

Zezhang Li [1], Shiqiao Gao [1,*], Lei Jin [2], Haipeng Liu [1] and Shaohua Niu [1]

[1] State Key Laboratory of Explosion Science and Technology, Beijing Institute of Technology, Beijing 100081, China; zezhang_li@163.com (Z.L.); lhp@bit.edu.cn (H.L.); shh@bit.edu.cn (S.N.)
[2] School of Mechatronical Engineering, Beijing Institute of Technology, Beijing 100081, China; jinlei@bit.edu.cn
* Correspondence: gaoshq@bit.edu.cn; Tel.: +86-10-6891-1631

Received: 10 July 2020; Accepted: 1 August 2020; Published: 3 August 2020

Abstract: A new micromachined vibrating ring gyroscope (VRG) architecture with low quadrature error and high-linearity is proposed, which successfully optimizes the working modes to first order resonance mode of the structure. The improved mode ordering can significantly reduce the vibration sensitivity of the device by adopting the hinge-frame mechanism. The frequency difference ratio is introduced to represent the optimization effect of modal characteristic. Furthermore, the influence of the structural parameters of hinge-frame mechanism on frequency difference ratio is clarified through analysis of related factors, which contributes to a more effective design of hinge-frame structure. The designed VRG architecture accomplishes the goal of high-linearity by using combination hinge and variable-area capacitance strategy, in contrast to the conventional approach via variable-separation drive/sense strategy. Finally, finite element method (FEM) simulations are carried out to investigate the stiffness, modal analysis, linearity, and decoupling characteristics of the design. The simulation results are sufficiently in agreement with theoretical calculations. Meanwhile, the hinge-frame mechanism can be widely applied in other existing ring gyroscopes, and the new design provides a path towards ultra-high performance for VRG.

Keywords: vibrating ring gyroscope; high-linearity; quadrature error; improved mode ordering; hinge-frame mechanism

1. Introduction

Due to the advantages on miniaturization, lightweight, easy integration, mass-production, and low-power consumption, the micro-electro-mechanical system (MEMS) vibrating gyroscope has become a significantly attractive device in a wide range of applications including automotive industry, biotechnology, medicine, space as well as consumer electronics [1–3]. Compared with tuning fork gyroscope (TFG), vibrating ring gyroscope (VRG) has the following advantages: (1) the sensitivity of the sensor is amplified by the quality factor due to the driving and sensing modes having identical frequency when the structures are fabricated from isotropic materials [4,5]. (2) It is less sensitive to temperature variations because thermal environment affects the identical vibrational modes of resonant rings equally [6,7]. (3) It is robust against random vibration since external vibrations do not couple to the identical vibration modes of rings [4,7–9].

A typical VRG consists of a ring structure, support beams and electrodes surrounding the ring structure. The electrodes are used for drive, sense, or control of the gyro. The operation of the ring gyroscope relies on two elliptically shaped vibration modes (flexural modes) [4,5,9–15]. The study of VRG has been widely reported in the literature. Michael William Putty et al. firstly developed

and fabricated the VRG with an open-loop sensitivity of 200 μV/°/s in a dynamic range of ±250 °/s under a low vacuum level [4,5]. Based on the design concept mentioned above, several variations of the architecture were also reported in the literature [10–15]. Meanwhile, much effort was already made to improve the gyroscope performance, including high shock reliability [7,9,16], parametric amplification [17–19], electrostatic tuning [20–22] and so on.

It is obvious that the limited dynamic range of VRGs (around ±250 °/s) mentioned above is insufficient to meet the demand for tactical applications. The original sources of the limited full-scale range are the quadrature error and the parallel-plate sensing mechanism assumed to be linear consisting of fixed electrodes and the outer circumference of the ring. The device vibration is mostly linear at normally used levels, however, the nonlinear jump that occurs at higher vibration level will restrict the application of ring gyroscope in higher requirements [4]. Some researchers focus on modelling of nonlinearities and control of nonlinear vibration [23–28]. On the other hand, much work has been done in decoupling the drive and sense modes, in order to minimize the quadrature error. The quadrature error can be largely eliminated at low vibration levels [20–22], while the drive/sense strategy remains the same and the improvement of the decoupling is extremely limited.

The vibration-induced error caused by poor mode ordering not only exists in TFG but also in VRG [29–31]. The resonant frequencies of translation modes in previous ring gyroscope designs are much smaller than those of the flexural modes (i.e., working modes). Detailed theoretical derivation by Sang Won Yoon et al. demonstrated that ring gyroscopes with non-proportional damping were not immune from external vibration. Therefore, the translation modes are more susceptible to external/environmental vibration whose frequency spectrum also lies well below resonant frequencies of flexural modes [8,32].

The hinge mechanisms with the advantage of rotation characteristic have attracted much attention and applied in MEMS devices, such as MEMS TFG, MEMS accelerometer and ring coupled gyroscope (RCG) [33–35]. The in-plane, n = 3 mode RCG designs of hinge mechanism have been adopted to increase the capacitive transduction areas by means of the auxiliary arrayed transducers. However, little attention has been paid to the principle of mode ordering improvement of VRG with hinge mechanisms. Besides, hinge mechanism on the optimization of decoupling and linearity of VRG is rarely reported.

In this paper, a novel designed vibrating ring gyroscope with a hinge-frame mechanism (HFVRG) is proposed. The structural characteristics and advantages of a HFVRG are introduced in Section 2. Section 3 establishes dynamic equations and discusses the modal characteristics as well as theoretical calculation. Finite element method (FEM) simulation of the stiffness of different springs and comparisons between simulation and theoretical results are discussed, and the linearity of the design is analyzed in Section 4. In Section 5, the discussions are given. Section 6 concludes the paper with a summary.

2. Architecture Design

The typical VRG, shown in Figure 1, consists of a ring structure, eight semicircular elastic support beams and electrodes. These electrodes can be sense, drive or control electrodes. Under the normal working condition of the VRG, the ring structure is forced to vibrate at the drive mode resonant frequency of the device along the green imaginary line. At higher vibration level, nonlinear jump phenomenon in sense capacitance of the sense electrode will lead to a stronger nonlinear response of the whole system.

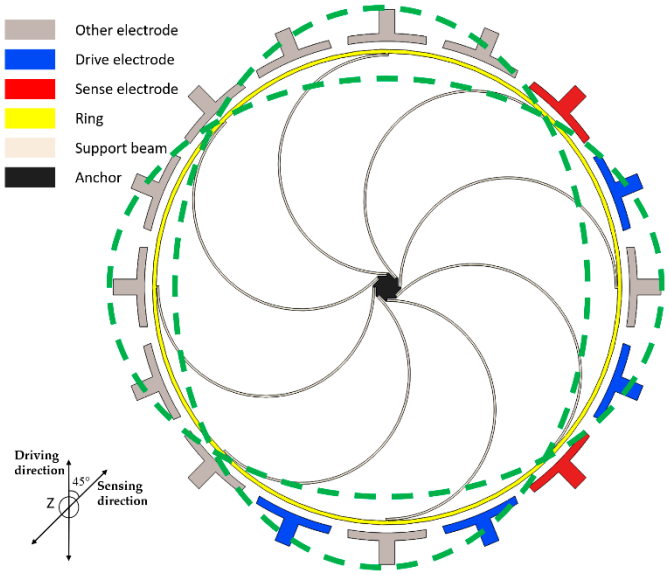

Figure 1. Schematic view of a typical vibrating ring gyroscope.

As mentioned above, typical VRG designs that possess translation modes have natural frequencies that are much smaller than those of flexural modes. As an intuitive quantitative consideration, Workbench is used to simulate the flexural mode and translation mode of the typical VRG shown in Figure 1 with radius, height and width of 1500 μm, 80 μm and 25 μm, respectively. The simulation results in Figure 2 illustrate that the frequencies of translation modes lie well below those of the flexural modes. Undoubtedly, this ring gyroscope is more impressionable to environmental vibration.

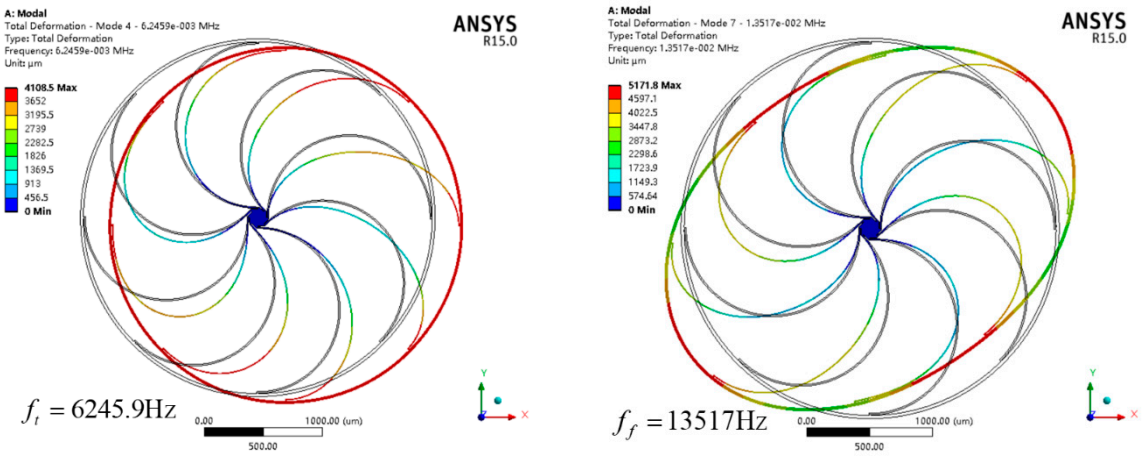

(**a**) (**b**)

Figure 2. Modal analysis of the translation mode (**a**) and flexural mode (**b**) of a typical vibrating ring gyroscope.

In order to eliminate the effects of nonlinear response and poor mode ordering, a novel vibrating ring gyroscope with a hinge-frame mechanism as drive/sense frame is designed, see Figure 3. The HFVRG is mainly composed of a ring structure, 8 semicircular elastic support beams, 8 hinge beams, 32 drive/sense beams, 8 drive/sense frames, and 8 groups of drive/sense electrodes. It is noteworthy that the resonant ring and support beams of HFVRG are identical to those of the typical VRG in Figure 1. The advantages of this design include:

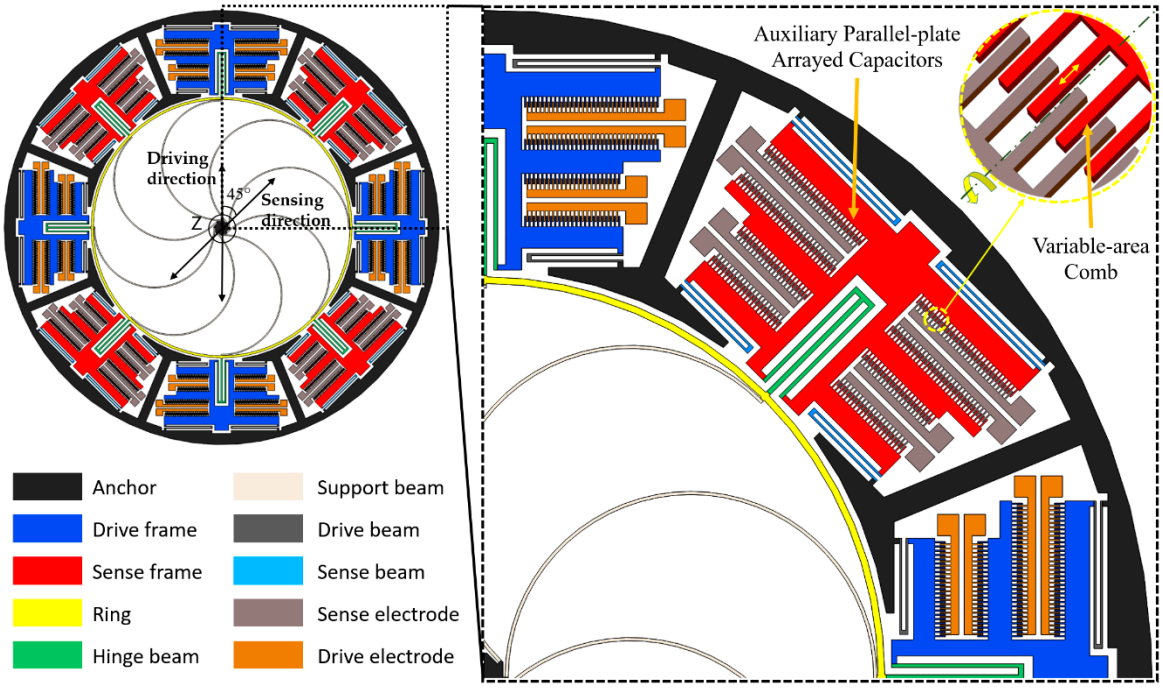

Figure 3. Schematic of vibrating ring gyroscope with a hinge-frame mechanism.

(1). The hinge beams can realize the rotation function and enable effect decouple between the drive mode and sense mode. The capacitance nonlinearity generated by capacitance change between the ring and the pickoff electrode in a typical VRG can be eliminated through variable-area comb mechanism.

(2). The hinge beams are located at the maximum radial displacement of the resonant ring to realize electromechanical coupling efficiently between the mechanical ring vibration and the electrical signal of drive/sense electrodes. Furthermore, the drive/sense electrodes with auxiliary parallel-plate arrayed capacitors are adopted to increase the capacitive transduction areas remarkably.

(3). The geometric symmetry structure between the ring and the anchor contributes to releasing the structural stress in the fabrication process.

3. Theoretical Analysis

The HFVRG operates as follows. The primary flexural (drive) mode is driven into resonance by driving voltages imposed on the drive electrodes of variable-area along the driving direction. When the device is subjected to rotation, a proportion of the vibration energy is converted from the primary flexural (drive) mode to the secondary flexural (sense) mode. Then vibration occurs in the sense direction due to the Coriolis effect. The amplitude of movable parallel plate displacement on the sense frame is proportional to the angular rate. Based on the principle, the angular rate of rotation is measured by detecting the displacement. As is depicted in Figure 3.

The stiffness of the support beams, hinge beams and drive/sense beams in the design of this paper are much less than those of drive/sense frames. On the other hand, the mass of the frames is larger than that of the beams. Therefore, the drive/sense frames are simplified to inelastic mass. Considering that the stiffness and mass of the vibrating ring structure are distributed along the ring, each beam is represented as a discrete spring attached to the drive/sense frame or ring mass and the ring is represented as a continuous (curved) beam.

3.1. Normal Modes of HFVRG

As described above, the MEMS HFVRG has two working modes: the primary flexural (drive) mode and the secondary flexural (sense) mode. Additionally, a more common translational vibration induced by environmental vibrations may also excite other in-the-plane modes. Particularly, the two

modes of ring translation cause a rigid translation of the ring on its support beams. Therefore, the overall motion of the ring can be decomposed into the motions that are excited by the gyroscope's operation (flexural modes) and the environment vibration (in-the-plane translation modes). In the present model, it was assumed that the ring performs in-plane motion only, and the out of plane motion was neglected [8,32].

Vibrating ring structure can be analyzed using normal modes. This analysis strategy is based on the fact that any plane vibration-induced displacement of the ring u can be demonstrated as the linear combination of its flexural modes (φ_1 and φ_2) and translation modes (φ_3 and φ_4). The total displacement of the ring structure is given by:

$$u = u(t, \theta) = \sum_{i=1}^{4} \varphi_i(\theta) q_i(t) \tag{1}$$

where θ is the independent spatial coordinate(s), and $q_i(t)$ are the generalized (modal) coordinates of the dynamic model of HFVRG.

The horizontal and vertical displacement of ring(u_x and u_y) are governed by:

$$\begin{aligned} u_x &= \varphi_{x1} q_1 + \varphi_{x2} q_2 + \varphi_{x3} q_3 + \varphi_{x4} q_4 \\ u_y &= \varphi_{y1} q_1 + \varphi_{y2} q_2 + \varphi_{y3} q_3 + \varphi_{y4} q_4 \end{aligned} \tag{2}$$

where Equation (2) is the Cartesian coordinate form of Equation (1). φ_{x1}, φ_{x2}, φ_{x3}, φ_{x4}, φ_{y1}, φ_{y2}, φ_{y3}, and φ_{y4} are the horizontal and vertical components of four plane modes in Cartesian coordinate system.

The mode shapes of a ring structure can be derived from simple calculations taking advantage of the symmetry of the ring structure [32]. The two elliptical-shaped flexural modes and two in-the-plane translation modes with Cartesian components are given by:

$$\text{Drive} - \text{axis flexural mode} : \varphi_{x1} = \left[\frac{1}{4}\cos(3\theta) + \frac{3}{4}\cos(\theta)\right],\ \varphi_{y1} = \left[\frac{1}{4}\sin(3\theta) - \frac{3}{4}\sin(\theta)\right] \tag{3}$$

$$\text{Sense} - \text{axis flexural mode} : \varphi_{x2} = \left[\frac{1}{4}\sin(3\theta) + \frac{3}{4}\sin(\theta)\right],\ \varphi_{y2} = \left[-\frac{1}{4}\cos(3\theta) + \frac{3}{4}\cos(\theta)\right] \tag{4}$$

$$\text{X} - \text{axis translation mode} : \varphi_{x3} = 1,\ \varphi_{y3} = 0 \tag{5}$$

$$\text{Y} - \text{axis translation mode} : \varphi_{x4} = 0,\ \varphi_{y4} = 1 \tag{6}$$

3.2. System Equations of HFVRG

The system equations of motion of HFVRG are derived in the literature by formulating the mechanical potential energy, kinetic energy, electrical potential energy, and energy dissipation by viscous damping, and employing Lagrange's method [8,32]. The four degree-of-freedom dynamical equation is as follows.

$$\begin{matrix} \text{mass} \\ \begin{bmatrix} M_1 & & & \\ & M_2 & & \\ & & M_3 & \\ & & & M_4 \end{bmatrix} \end{matrix} \begin{Bmatrix} \ddot{q}_1 \\ \ddot{q}_2 \\ \ddot{q}_3 \\ \ddot{q}_4 \end{Bmatrix} + \begin{matrix} \text{damping} \\ \begin{bmatrix} c_{11} & & & \\ & c_{22} & & \\ & & c_{33} & \\ & & & c_{44} \end{bmatrix} \end{matrix} \begin{Bmatrix} \dot{q}_1 \\ \dot{q}_2 \\ \dot{q}_3 \\ \dot{q}_4 \end{Bmatrix} + \begin{matrix} \text{Coriolis couping} \\ \begin{bmatrix} 0 & -2\gamma_1\Omega_z & & \\ 2\gamma_1\Omega_z & 0 & & \\ & & 0 & -2\gamma_2\Omega_z \\ & & 2\gamma_2\Omega_z & 0 \end{bmatrix} \end{matrix} \begin{Bmatrix} \dot{q}_1 \\ \dot{q}_2 \\ \dot{q}_3 \\ \dot{q}_4 \end{Bmatrix} +$$
$$\begin{matrix} \text{angular acceleration} \\ \begin{bmatrix} 0 & -\gamma_1\dot{\Omega}_z & & \\ \gamma_1\dot{\Omega}_z & 0 & & \\ & & 0 & -\gamma_2\dot{\Omega}_z \\ & & \gamma_2\dot{\Omega}_z & 0 \end{bmatrix} \end{matrix} \begin{Bmatrix} q_1 \\ q_2 \\ q_3 \\ q_4 \end{Bmatrix} - \Omega_z^2 \begin{matrix} \text{centripetal stiffness} \\ \begin{bmatrix} M_1 & & & \\ & M_2 & & \\ & & \alpha_1 & \\ & & & \beta_2 \end{bmatrix} \end{matrix} \begin{Bmatrix} q_1 \\ q_2 \\ q_3 \\ q_4 \end{Bmatrix} + \begin{matrix} \text{stiffness} \\ \begin{bmatrix} k_1 & & & \\ & k_2 & & \\ & & k_3 & \\ & & & k_4 \end{bmatrix} \end{matrix} \begin{Bmatrix} q_1 \\ q_2 \\ q_3 \\ q_4 \end{Bmatrix} = \begin{matrix} \text{drive force} \\ \begin{Bmatrix} f_1 \\ f_2 \\ f_3 \\ f_4 \end{Bmatrix} \end{matrix} \tag{7}$$

where

$$M_1 = \int_V \rho\left[(\varphi_{x1})^2 + \left(\varphi_{y1}\right)^2\right]dV + 4m_f,\ M_2 = \int_V \rho\left[(\varphi_{x2})^2 + \left(\varphi_{y2}\right)^2\right]dV + 4m_f$$
$$M_3 = \int_V \rho\left[(\varphi_{x3})^2 + \left(\varphi_{y3}\right)^2\right]dV + 2m_f,\ M_4 = \int_V \rho\left[(\varphi_{x4})^2 + \left(\varphi_{y4}\right)^2\right]dV + 2m_f \quad (8)$$

$$\gamma_1 = \int_V \rho\left[\varphi_{x3}\varphi_{y3}\right]dV,\ \gamma_2 = \int_V \rho\left[\varphi_{x3}\varphi_{y4} - \varphi_{x4}\varphi_{y3}\right]dV,\ \alpha_1 = \int_V \rho(\varphi_{x3})^2 dV,\ \beta_2 = \int_V \rho\left(\varphi_{y4}\right)^2 dV \quad (9)$$

$$K_F = K_{ri} + 4K_{hs} + 8K_{dsy1} + 8K_{dsy2},\ K_T = 2K_{hs} + 2K_{vs} + 4K_{45} + 2K_{hx} + 4K_{dsy1} + 4K_{dsy2} \quad (10)$$

$$K_{ri} = 10\pi\frac{EI}{r_r^3}(i = 1,2),\ K_{ns} = \frac{2\pi EI_s}{(\pi^2 - 8){r_s}^3}, K_{ts} = \frac{2EI_s}{\pi {r_s}^3}, K_{45} = \frac{2\left(\pi^2 - 4\right)EI_s}{\pi(\pi^2 - 8){r_s}^3} \quad (11)$$

Here, $M_i(i = 1,2)$ describes the modal mass associated with the flexural modes of HFVRG. m_f is the mass of the drive/sense frame. ρ and V represent the density and volume of the ring structure, respectively. $M_i(i = 3,4)$ describes the modal mass associated with the translation modes of the architecture. The quantities γ_1 and γ_2 denote respectively a modal coupling induced by the Coriolis force and angular acceleration, and the quantities α_1 and β_2 indicate additional stiffness induced by the centripetal acceleration. $c_{ii}(i = 1,2,3,4)$ are the modal damping coefficients. k_1 and k_2 are the modal stiffnesses of two flexural modes of HFVRG (K_F herein). k_3 and k_4 are the modal stiffnesses of two translation modes of the design (K_T herein). $K_{ri}(i = 1,2)$ are the equivalent stiffnesses of ring structures associated with two flexural modes. K_{hs}, K_{vs}, and K_{45} are the horizontal stiffness, the vertical stiffness and the stiffness along to the 45° direction of the semicircular elastic support beam, respectively. As shown in Figure 4. E is the elastic modulus of the silicon material. I and I_s represent respectively the second moment of area of the ring cross-section and support beam cross-section. It is necessary to point out that the (111) silicon wafer was found to be in-plane isotropic in the literature [36,37]. r_r and r_s are the radius of the ring structure and semicircular elastic support beam, respectively. Mentioning that the pairs of modal masses and modal stiffnesses are identical if the ring gyroscope is uniform and axisymmetric (i.e., ideally fabricated). In addition, K_{dsy1} and K_{dsy1} are the stiffness of the drive/sense beam near and away from the resonant ring, respectively. K_{hx} is the stiffness of the hinge beam.

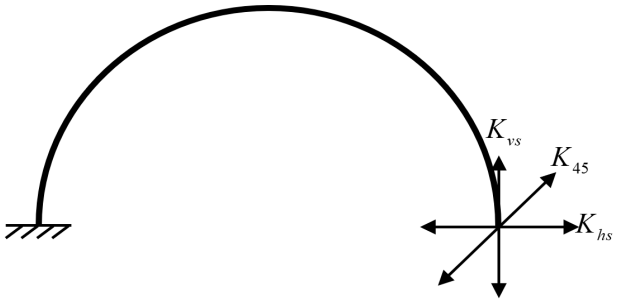

Figure 4. Stiffnesses of a semicircular elastic support beam in three directions.

3.3. The Stiffness Analysis of Drive/Sense Beam and Hinge Beam

The elastic beams with a large length and relatively small flexural strength such as hinge beams and drive/sense beams can be analyzed using a lumped-parameter model. On the other hand, the drive/sense beams and hinge beams in the design are U-shaped in series or in parallel, which can reduce their axial stress to some extent. Hence, there is a linear relationship between force and displacement. Energy principles in structural mechanics will be used to derive the stiffness of hinge beams and drive/sense beams.

The drive/sense beam is composed of three rectangular beams, as shown in Figure 5. The stiffness characteristics of drive/sense beams are explored using the Castigliano's second theorem and the

derivation is described in detail in Appendix A. The stiffness of drive/sense beam in the direction of x-axis and y-axis can be written as:

$$K_{dsy} = \frac{E}{D},\ K_{dsx} = \frac{E}{H} \tag{12}$$

where

$$\begin{gathered}
D = \frac{\left(\begin{array}{l} I_1I_2l_3\left((A+l_2)^2C^2+(A+l_2)(2B-2l_1+l_3)C+l_1^2-(2B+l_3)l_1+l_3^2/3+l_3B+B^2\right)+ \\ I_1I_2I_3\left(\left(A^2+l_2A+l_2^2/3\right)C^2+C(2A+l_2)(B-l_1)+(B-l_1)^2\right)+l_1I_2I_3\left(A^2C^2+AC(2B-l_1)+B^2-l_1B+l_1^2/3\right)\end{array}\right)}{I_1I_2I_3}, \\
H = \frac{\left(\begin{array}{l} I_1I_2l_3\left(\left(l_1^2-(2B+l_3)l_1+l_3^2/3+Bl_3+B^2\right)G^2+(A+l_2)(2B-2l_1+l_3)G+(A+l_2)^2\right)+ \\ I_1I_2I_3\left((B-l_1)^2G^2+(2A+l_2)(B-l_1)G+\left(A^2+Al_2+l_2^2/3\right)\right)+l_1I_2I_3\left(\left(B^2-Bl_1+l_1^2/3\right)G^2+AG(2B-l_1)+A^2\right)\end{array}\right)}{I_1I_2I_3} \\
C = -\frac{I_1I_2l_3(A+l_2)(B-l_1+l_3/2)+I_1I_2I_3(A+l_2/2)(B-l_1)+l_1I_2I_3A(B-l_1/2)}{I_1I_2l_3(A+l_2)^2+I_1I_2I_3\left(A^2+l_2A+l_2^2/3\right)+l_1I_2I_3A^2} \\
G = -\frac{I_1I_2l_3(A+l_2)(B-l_1+l_3/2)+I_1I_2I_3(A+l_2/2)(B-l_1)+l_1I_2I_3A(B-l_1/2)}{I_1I_2l_3\left(l_1^2-(2B+l_3)l_1+B^2+Bl_3+l_3^2/3\right)+I_1I_2I_3(B-l_1)^2+l_1I_2I_3\left(B^2-Bl_1+l_1^2/3\right)} \\
A = -\frac{I_1I_2(2I_2I_3+I_2I_3)}{2(I_1I_2I_3+I_1I_2I_3+I_1I_2I_3)},\ B = \frac{I_1I_2I_3(2I_1-I_3)+I_1I_3(2I_1I_2+I_1I_2)}{2(I_1I_2I_3+I_1I_2I_3+I_1I_2I_3)}
\end{gathered} \tag{13}$$

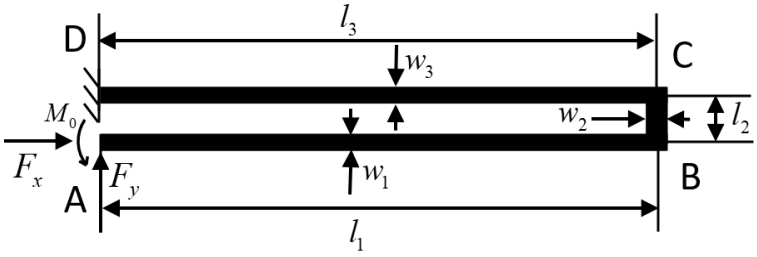

Figure 5. Structure schematic diagram of drive/sense beam.

Figure 6a displays the structure schematic diagram of the hinge beam. It can be seen that the hinge beam consists of three parts and can be simplified to the lumped model shown in Figure 6b, where the stiffness characteristics of k_{h2} are exactly the same as those of k_{h3}. The stiffness characteristics of hinge beams are investigated using the same strategy as those of driving (or sense) beams. According to the previous analysis, the stiffness of the hinge beam in the direction of x-axis and y-axis can be written as:

$$k_{hx} = \frac{2k_{h1x}k_{h2x}}{2k_{h2x}+k_{h1x}},\ k_{hy} = \frac{2k_{h1y}k_{h2y}}{2k_{h2y}+k_{h1y}} \tag{14}$$

where

$$k_{h1x} = \frac{E}{D_1},\ k_{h1y} = \frac{E}{H_1}, k_{h2x} = \frac{E}{D_2},\ k_{h2y} = \frac{E}{H_2} \tag{15}$$

$$\begin{gathered}
D_1 = \frac{\left({A_1}^2+A_1l_4+l_4^2/3\right)l_4}{I_4},\ H_1 = 0,\ A_1 = -\frac{l_4}{2},\ A_2 = \frac{I_5l_6^2}{2(I_5l_6+I_6l_5)}, B_2 = -\frac{2I_5l_5l_6+I_6l_5^2}{2(I_5l_6+I_6l_5)} \\
D_2 = \frac{\left(\begin{array}{l}\left(I_5l_6(B_2+l_5)^2+I_6l_5\left(B_2^2+l_5B_2+l_5^2/3\right)\right)C_2^2+\left(l_6A_2^2-l_6^2A_6+l_6^3/3\right)I_5 \\ +I_6l_5A_2^2+(2I_5l_6(A_2-l_6/3)(B_2+l_5)+I_6l_5A_2(2B_2+l_5))C_2\end{array}\right)}{I_5I_6} \\
H_2 = \frac{\left(\begin{array}{l} I_5l_6\left(l_5^2+l_5(2A_2G_2+2B_2-G_2l_6)+G_2^2l_6^2/3-l_6\left(B_2G_2+A_2G_2^2\right)+(A_2G_2+B_2)^2\right) \\ +I_6l_5\left((A_2G_2+B_2)^2+l_5(A_2G_2+B_2)+l_5^2/3\right)\end{array}\right)}{I_5I_6} \\
C_2 = -\frac{6I_5l_6A_2B_2+6I_6l_5A_2B_2+6I_5l_5l_6A_2+3I_6l_5^2A_2-3I_5l_6^2B_2-3I_5l_5l_6^2}{6B_2^2I_5l_6+6B_2^2I_6l_5+12B_2I_5l_5l_6+6B_2I_6l_5^2+6I_5l_5^2l_6+2I_6l_5^3} \\
G_2 = -\frac{6I_5l_6(B_2+l_5)(A_2-l_6/2)+3I_6l_5A_2(2B_2+l_5)}{\left(6l_6A_2^2-6l_6^2A_2+2l_6^3\right)I_5+6I_6l_5A_2^2}
\end{gathered} \tag{16}$$

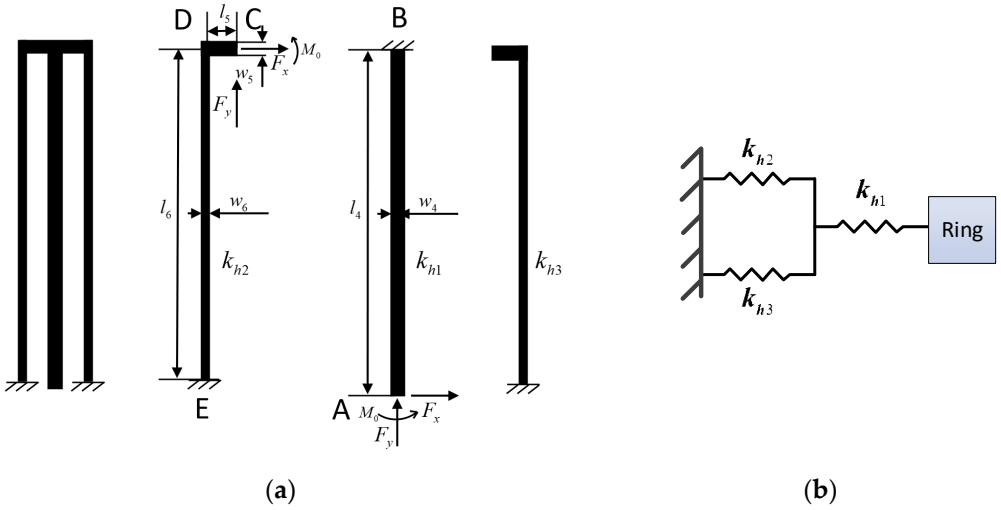

Figure 6. Structure schematic diagram (**a**) and lumped model (**b**) of the hinge beam.

3.4. Discussion of Resonant Frequency and FDR

The developed dynamical model concerning the HFVRG can be utilized to further predict the resonant frequencies of flexural modes and translation modes of the sensor. At typical working frequencies of the HFVRG, the angular acceleration term and centrifugal stiffness will not cause too much change and can be neglected. The natural frequencies for four normal modes are given by the simple relationships.

$$f_f = \frac{1}{2\pi}\sqrt{\frac{k_i}{M_i}}(i = 1,2),\ f_t = \frac{1}{2\pi}\sqrt{\frac{k_i}{M_i}}(i = 3,4) \tag{17}$$

where f_f and f_t are the resonant frequencies of the flexural modes and translation modes in HFVRG, respectively.

In order to further investigate the optimization effect of each key parameter (mass parameter and stiffness parameter) on the mode ordering, the dimensionless parameter η is defined by:

$$\eta = \frac{f_t - f_f}{f_f} \tag{18}$$

where η is defined as the frequency difference ratio (FDR) denoting the ratio of the frequency difference between translation and flexural modes to the resonant frequency of flexural mode.

Substituting Equations (8), (10) and (17) into Equation (18), we obtain:

$$\eta = \sqrt{\frac{(k_{ns} + k_{ts})\left(5m_r + 32m_f\right)}{8(k_r + 2k_{ns})\left(m_r + 2m_f\right)}} - 1 \tag{19}$$

where $k_{ns} = 2K_{ns} + 4K_{dsy1} + 4K_{dsy2}$ and $k_{ts} = 2K_{ts} + 2K_{hx} + 4K_{45}$ represent the normal stiffness and tangential stiffness of the whole structure, respectively. $k_r = K_{ri}$ and m_r represent modal stiffness of resonant ring associated with two flexural modes and the mass of the ring structure, respectively.

It can be seen that the FDR is mainly determined by the stiffness parameters k_{ns}, k_{ts} and k_r as well as mass parameters m_r and m_f. By solving the partial derivative of function η with respect to these variables, we obtain that:

$$\frac{\partial \eta}{\partial k_{ns}} = \frac{\sqrt{2\left(5m_r + 32m_f\right)}(k_r - 2k_{ts})}{8\sqrt{(k_{ns} + k_{ts})\left(m_r + 2m_f\right)(k_r + 2k_{ns})^3}} \tag{20}$$

$$\frac{\partial \eta}{\partial k_{ts}} = \frac{\sqrt{2\left(5m_r + 32m_f\right)}}{8\sqrt{(k_{ns} + k_{ts})\left(m_r + 2m_f\right)(k_r + 2k_{ns})}} \tag{21}$$

$$\frac{\partial \eta}{\partial k_r} = -\frac{\sqrt{2(k_{ns} + k_{ts})\left(5m_r + 32m_f\right)}}{\sqrt{\left(m_r + 2m_f\right)(k_r + 2k_{ns})^3}} \tag{22}$$

$$\frac{\partial \eta}{\partial m_r} = -\frac{11m_f\sqrt{2(k_{ns} + k_{ts})}}{4\sqrt{\left(5m_r + 32m_f\right)\left(m_r + 2m_f\right)^3(k_r + 2k_{ns})}} \tag{23}$$

$$\frac{\partial \eta}{\partial m_f} = \frac{11m_r\sqrt{2(k_{ns} + k_{ts})}}{4\sqrt{\left(5m_r + 32m_f\right)\left(m_r + 2m_f\right)^3(k_r + 2k_{ns})}} \tag{24}$$

In general, the values of the stiffness parameters k_{ns}, k_{ts} and k_r as well as mass parameters m_r and m_f are greater than 0. From Equations (21)–(24), we can find that:

$$\frac{\partial \eta}{\partial k_{ts}} > 0,\ \frac{\partial \eta}{\partial k_r} < 0,\ \frac{\partial \eta}{\partial m_r} < 0,\ \frac{\partial \eta}{\partial m_f} > 0 \tag{25}$$

From Equation (25), the FDR η monotonically increases with increasing k_{ts} and m_f, but decreases with increasing k_r and m_r. Within a reasonable range, k_r and m_r are as small as possible and k_{ts} and m_f are as large as possible; the FDR can be improved effectively and the effect of translation vibration on the performance of ring gyroscope can be eliminated effectively.

From Equation (20), it appears that the influence of the normal stiffness of the whole device on FDR depends on the difference between the flexural modal stiffness of resonant ring and the two times tangential stiffness of the design. Therefore, we conclude that under the premise of $k_r - 2k_{ts} < 0$, the FDR decreases with increasing the normal stiffness of the whole device.

The aforementioned VRG with different forms of supporting beams often provided poor modal ordering. It can be remarked that the hinge-frame mechanism we proposed can change the modal ordering of original ring gyroscope and is expected to be applied to all kinds of existing ring gyroscopes. Here, four architectures based on HFVRG are designed to explore the impact of the parameters of hinge-frame mechanism such as K_{hx}, K_{dsy} and m_f on FDR, defined as types A, B, C, and D. The K_{hx} of type B, the m_f of type C and the K_{dsy} of type D are slightly larger than those of type A. This can be achieved by intentionally decreasing the spring width of the hinge beam and drive/sense beam as well as the volume of drive/sense frame, respectively.

3.5. Theoretical Calculation

The critical parameters of the geometric and material properties of the HFVRG in the designs and FEM simulation stage are shown in Tables 1 and 2, respectively.

These parameters are substituted into the previous equation, and the main theoretical stiffness, theoretical resonant frequencies of flexural modes and translation modes as well as FDR in all types can be obtained, as indicated in Table 3.

It can be seen that the theoretical resonant frequency of flexural mode is lower than that of translation mode in all types, which results in an excellent mode ordering. Furthermore, it is necessary to point out that the FDR of type A is higher than that of type B and C, and lower than that of type D from Table 3, which is consistent with previous analysis.

Table 1. Main parameters of the structures.

Parameter	Value
Radius of resonant ring in all types (r_r) (μm)	1500
Width of resonant ring in all types (w_r) (μm)	25
Radius of support beam in all types (r_s) (μm)	690
Width of support beam in all types (w_r) (μm)	12
Length of drive/sense beam 1 in type A, B and C [l_{11}, l_{21}, l_{31}] (μm)	[345,16,345]
Width of drive/sense beam 1 in type A, B and C [w_{11}, w_{21}, w_{31}] (μm)	[8,16,8]
Length of drive/sense beam 1 in type D [w_{11}, w_{21}, w_{31}] (μm)	[345,18,345]
Width of drive/sense beam 1 in type D [w_{11}, w_{21}, w_{31}] (μm)	[7,16,7]
Length of drive/sense beam 2 in all types [l_{12}, l_{22}, l_{32}] (μm)	[537,16,537]
Width of drive/sense beam 2 in all types [w_{12}, w_{22}, w_{32}] (μm)	[8,16,8]
Length of hinge beam in type A, C and D [l_4, l_5, l_6] (μm)	[505,30,485]
Width of hinge beam in type A, C and D [w_4, w_5, w_6] (μm)	[18,20,14]
Length of hinge beam in type B [l_4, l_5, l_6] (μm)	[505,32,485]
Width of hinge beam in type B [w_4, w_5, w_6] (μm)	[18,20,12]
Height of the whole structure in all types (h) (μm)	80
Mass of resonant ring in all types (m_r) (kg)	4.35×10^{-8}
Mass of drive/sense frame in type A, B and D (m_f) (kg)	6.94×10^{-8}
Mass of drive/sense frame in type C (m_f) (kg)	6.73×10^{-8}

Table 2. Material parameters for FEM simulation.

Parameter	Young's Modulus (Pa)	Poisson's Ratio	Density (kg/m^3)
Values	1.7×10^{11}	0.28	2330

Table 3. Main theoretical stiffness and theoretical resonant frequencies.

Parameter	Type A	Type B	Type C	Type D
Stiffness of resonant ring (K_r) (N/m)			164.75	
Normal stiffness of support beam (K_{ns}) (N/m)			20.13	
Tangential stiffness of support beam (K_{ts}) (N/m)			3.80	
The stiffness along to the 45° of support beam (K_{45}) (N/m)			11.96	
Stiffness of drive/sense beam 1 (K_{dsy1}) (N/m)	84.06	84.06	84.06	56.25
Stiffness of drive/sense beam 2 (K_{dsy2}) (N/m)			22.36	
Stiffness of hinge beam (K_{hx}) (N/m)	314.82	245.29	314.82	314.82
Resonant frequency of flexural mode of HFVRG (f_f) (Hz)	9551	9551	9685	8528
Resonant frequency of translation mode of HFVRG (f_t) (Hz)	12,652	11,863	12,800	12,025
Frequency difference ratio (FDR) (η)	32.46%	24.20%	32.16%	41.01%

4. FEM Simulation and Analysis

4.1. Analysis of Various Beams

From Equation (20), the modal stiffness is dependent on the stiffness of various beams in the designs. Therefore, simulations are carried out on the stiffness of these beams by applying a 1 μN force in the linked structure, as shown in Figure 7. The normal stiffness, tangential stiffness and the stiffness along to the 45° support beam are shown in Figure 7a–c, respectively. The stiffness of the hinge beam and the two drive/sense beams are shown in Figure 7d–f, respectively. Using the formula $k = F/x$, the stiffness can be obtained:

$$\begin{gathered} K_{ns} = \frac{1\ \mu\text{N}}{0.04972\ \mu\text{m}} = 20.11\ \text{N/m},\ K_{ts} = \frac{1\ \mu\text{N}}{0.36193\ \mu\text{m}} = 2.76\ \text{N/m} \\ K_{45} = \frac{1\ \mu\text{N}}{0.1113\ \mu\text{m}} = 8.98\ \text{N/m},\ K_{hx\_A\_C\_D} = \frac{1\ \mu\text{N}}{0.003165\ \mu\text{m}} = 315.96\ \text{N/m} \\ K_{hx\_B} = \frac{1\ \mu\text{N}}{0.004009\ \mu\text{m}} = 249.44\ \text{N/m},\ K_{dsy1\_A\_B\_C} = \frac{1\ \mu\text{N}}{0.011983\ \mu\text{m}} = 83.45\ \text{N/m} \\ K_{dsy1\_D} = \frac{1\ \mu\text{N}}{0.017716\ \mu\text{m}} = 56.45\ \text{N/m},\ K_{dsy2} = \frac{1\ \mu\text{N}}{0.045095\mu\text{m}} = 22.18\ \text{N/m} \end{gathered} \tag{26}$$

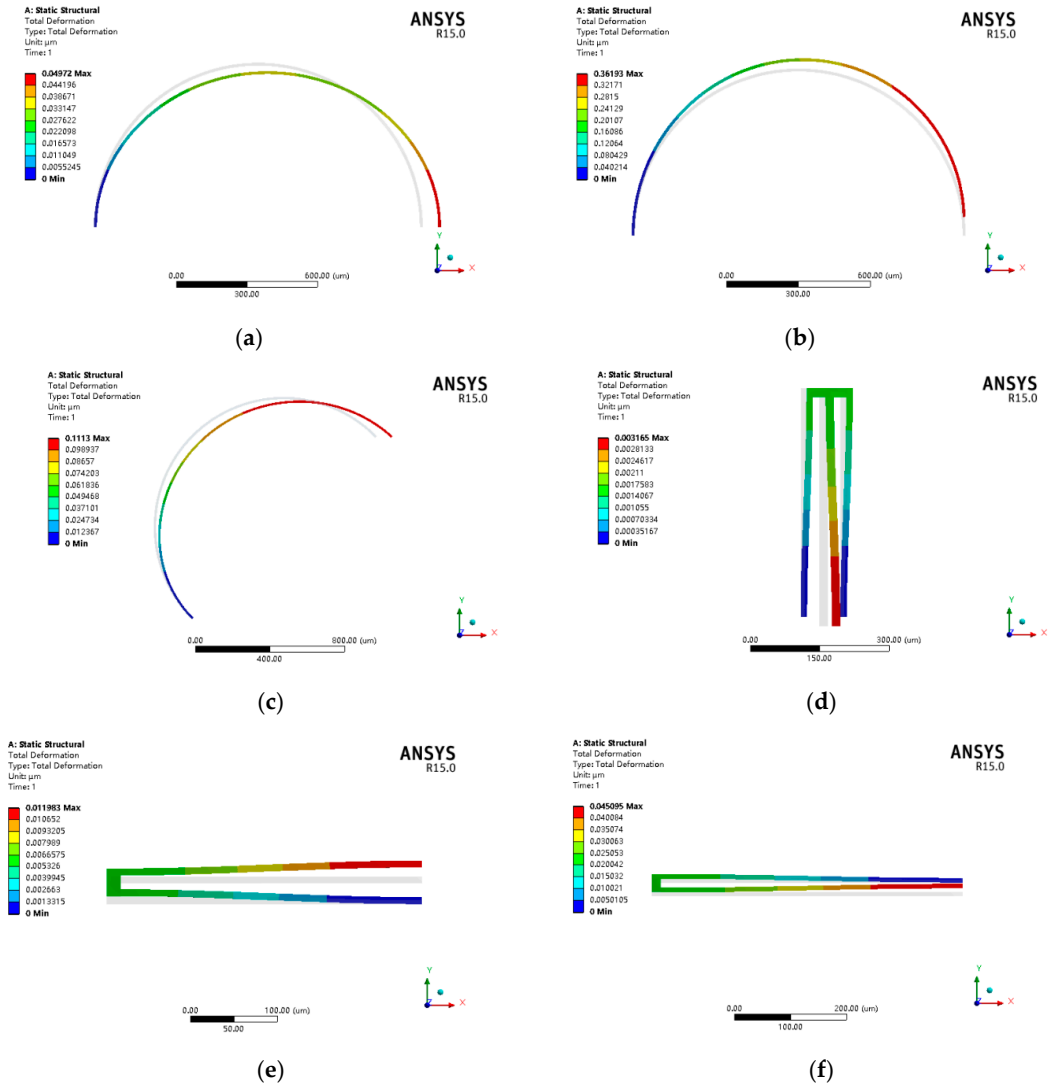

Figure 7. Stiffness of various beams of MEMS gyroscope: (**a**) deformation of K_{ns}; (**b**) deformation of K_{ts}; (**c**) deformation of K_{45}; (**d**) deformation of K_{lix}; (**e**) deformation of K_{dsy1}; (**f**) deformation of K_{dsy2}.

It can be seen that the stiffness of various beams by FEM from Equation (26) and Figure 7 is basically in accordance with the theoretical results depicted in Table 3, which verifies the proposed theoretical model.

4.2. Modal Analysis and Comparisons

Modal analysis can be applied to investigate the vibration characteristics of the device structure, such as the mode shape, resonant frequency and vibration stability. A more detailed structural model simulation is carried out by FEM using the commercial software ANSYS-Workbench. The mesh element is SOLID186, which is a high-order three-dimensional 20-node solid structure unit. All the structures use hexahedral meshes: the linear beam uses a small mesh, the drive/sense frames use slightly larger meshes, and all anchor uses larger hexahedral meshes. Types A, B, C, and D have a total of 586,872, 597,224, 586,040, and 587,704 nodes, respectively. The main parameters of the structures and the material properties of silicon are shown in Tables 1 and 2, respectively.

Figure 8 shows the flexural modal diagram and translation modal diagram of all types. It is necessary to point out that the two flexural modes of all types are the first two order modes and the two translation modes of them are the third and fourth modes. It can be seen that minor adjustment of structural parameters for hinge-frame mechanism cannot cause a change in the mode ordering.

Besides, this design can effectively improve the resonant frequency of disturbance modes such as torsional mode, out-of-plane translation mode and out-of-plane rocking mode compared with the original one. The natural frequencies of the flexural and translation modes and the FDR of all types are listed in Table 4.

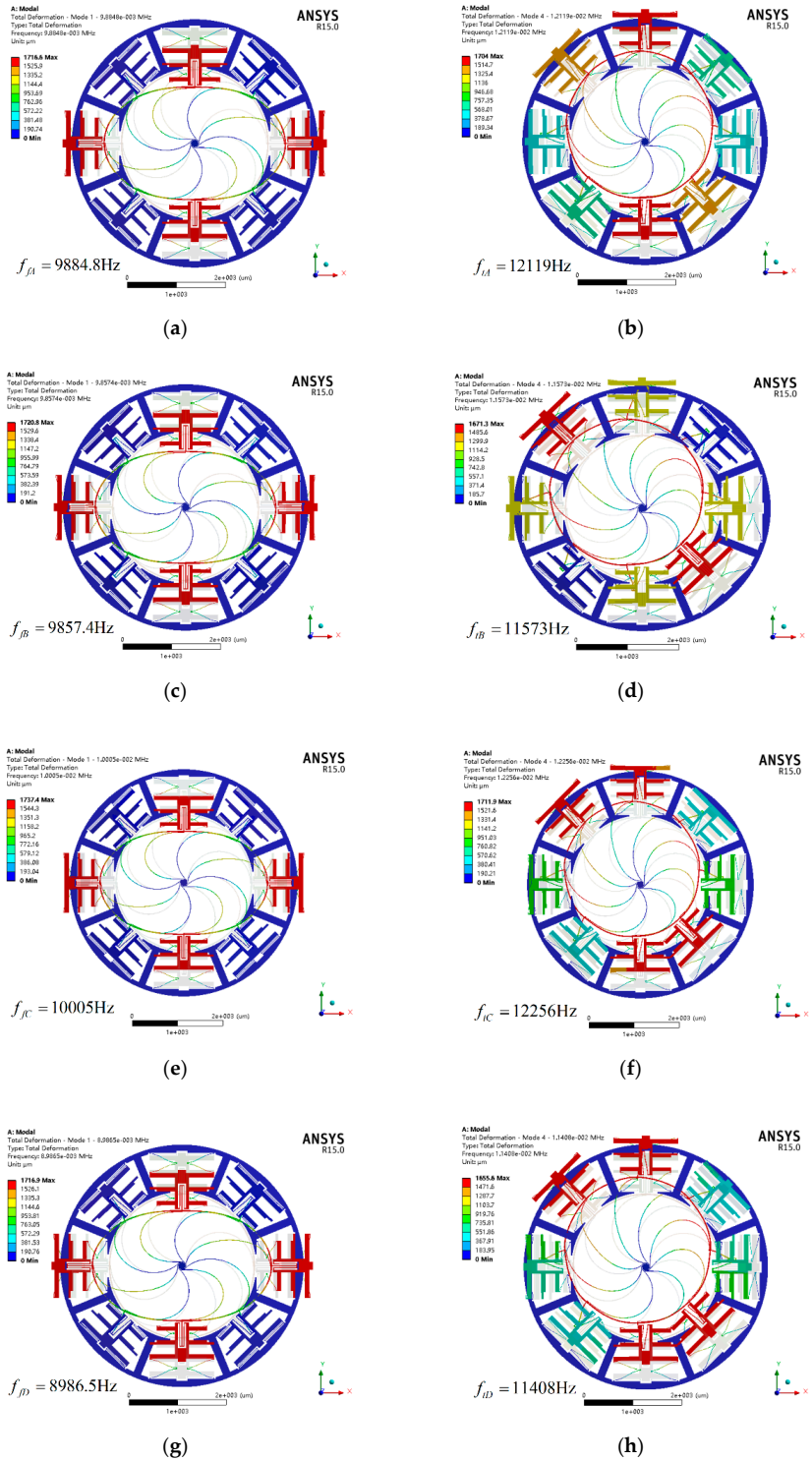

Figure 8. Flexural modal diagram (**a**), (**c**), (**e**), (**g**) and translation modal diagram (**b**), (**d**), (**f**), (**h**) of type A, B, C, and D.

Table 4. Natural frequencies of the flexural and translation modes and the FDR of all types.

Parameter	Type A	Type B	Type C	Type D
Resonant frequency of flexural mode (Hz)	9884.8	9857.4	10,005	8986.5
Resonant frequency of translation mode (Hz)	12,119	11,573	12,256	11,408
Frequency difference ratio (FDR)	22.60%	17.40%	22.50%	26.95%

It can be seen from Table 4 that the FDR of type A is higher than that of type B and C, and is lower than that of type D, which is in keeping with theoretical results in Section 3.5. The theoretical and simulation values of all types and the corresponding error rates are obtained and listed in Table 5.

Table 5. Comparison of theoretical and simulation values of types A, B, C, and D.

Type	Mode Shape	Theoretical Value	Simulation Value	Error Rate
Type A	Flexural mode	9551	9884.8	−3.50%
	Translation mode	12,652	12,119	4.21%
Type B	Flexural mode	9551	9857.4	−3.21%
	Translation mode	11,863	11,573	2.44%
Type C	Flexural mode	9685	10,005	−3.40%
	Translation mode	12,800	12,256	4.25%
Type D	Flexural mode	8528	8986.5	−5.38%
	Translation mode	12,025	11,408	5.13%

From Table 5, it can be found that the simulation results are consistent with the theoretical values in all types. In addition, the frequency of flexural mode is lower than that of translation mode in each type. Therefore, the proposed theoretical model is accurate and rational for the hinge-frame mechanism.

4.3. Nonlinear and Coupling Analysis

One of the driving and detecting errors neglected in the above simplified model is derived from the structure nonlinearity, which is caused by the large deformation of drive or sense beams. Therefore, a validation is provided here. Since most of the literatures have pointed out that the dominant signal in output signals is the quadrature error, it is necessary to further validate the advantage of decoupling and high linearity in the design with a simple analysis by FEM using ANSYS-Workbench.

The nonlinear analysis can be used to analyze problems where the stress–strain relationship of the material is nonlinear and check whether the model gives reasonable results or not. In this simulation, the parameters of the structure, material properties of silicon, mesh division and element type are the same as those of the modal analysis. The predefined environments (i.e., supports and loads) are shown in Figure 9a. It can be seen that all the anchors are set to the fixed support, and the equivalent force of 300 μN is applied at the antinode on the ring to simulate the deformation of the flexural mode. The total deformation with a magnification of 50 times is depicted in Figure 9b. We define that d_d is the displacement of drive frame, d_{sc} is the coupling displacement of sense frame and d_{rc} is the coupling displacement of node on resonant ring. For comparison purposes, d_{rc} is represented as the coupling displacement of sense electrodes in typical VRG.

From Table 1. It can be seen that the interval of drive/sense U-shape beam has a width of 16 μm (l_{21}). Therefore, the maximum displacement of the whole structure is 16 μm. After nonlinear analysis, the input equivalent force vs. output displacement of drive frame (d_d), sense frame (d_{sc}) and node of resonant ring (d_{rc}) as well as linear fit of measured data are shown in Figure 10.

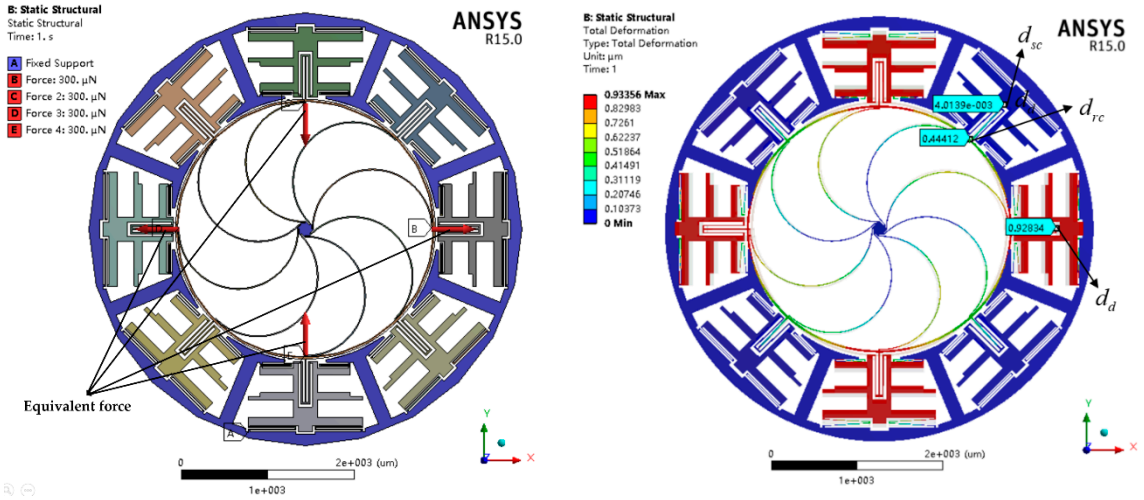

Figure 9. The predefined environments (**a**) and total deformation with a magnification of 50 times (**b**) when the equivalent force is 300 μN of nonlinear analysis.

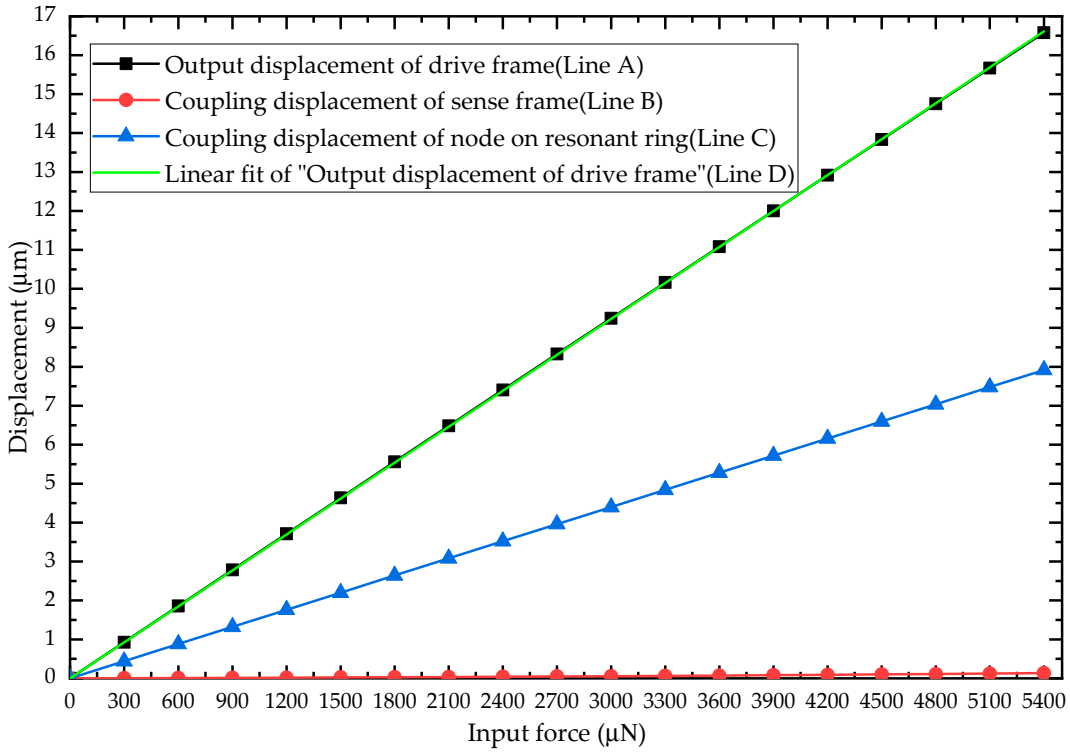

Figure 10. The output displacement of drive frame (Line A), sense frame (Line B) and node of resonant ring (Line C) at different input forces as well as linear fit of measured data (Line D).

As can be seen from Figure 10, the displacement of drive frame (Line A) and the node on resonant ring increases (Line C) almost linearly with the increase of the input force, and the displacement of drive frame (Line A) is about twice that of the node on the resonant ring (Line C). However, the displacement of sense frame (Line B) remains at a low level though it has a tendency to increase, which verifies that the design has an advantage of quadrature decoupling compared with the typical VRG. Additionally, in order to verify the linearity of the HFVRG in the maximum working range, the deviation from the best-fit line (Line D) is calculated. The structure nonlinearity caused by large deformation of drive or

sense beams is found to be negligible (adjusted $R^2 = 0.99999$), which verifies that the design works within a linear interval.

5. Discussion

It is noteworthy that there are still some errors in the theoretical results and simulation results of the resonant frequencies for both translation and flexural modes. This is due to the assumption that drive/sense beam as a one-dimensional linear spring in theoretical analysis. However, these errors have no effect on the final modal characteristics.

The present work is fundamental for the novel HFVRG, which focuses on the structure design and principle verification. Further research includes: (1) The investigation of high shock reliability will pay more attention to VRG architecture. (2) The proposed HFVRG will be fabricated through a conventional silicon-on-glass (SOG) and deep reactive ion etching (DRIE) process for experimental verification.

6. Conclusions

In this study, a high-linearity, low quadrature error and prefect mode ordering MEMS vibrating ring gyroscope with a hinge-frame mechanism is proposed. A systematic dynamic model is established to investigate the modal characteristics, and the FDR is introduced to characterize the optimization effect. The theoretical calculation results show that the FDR increases with increased tangential stiffness of the whole structure, while the mass of drive/sense frame decreases with increased normal stiffness of the whole structure under certain conditions. Four architectures based on HFVRG with different values of stiffness or mass are designed. In addition, the stiffness of all the four types of beams and modal analysis are carried out by FEM simulation, which demonstrates that the stiffness and modal characteristics of the design are in keeping with theoretical results. Furthermore, the nonlinearity analysis indicates that the HFVRG possesses high-linearity and decoupling characteristics. Consequently, the proposed HFVRG is capable to offer a high linearity excitation and detection strategy, improved mode ordering and eliminate the quadrature coupling effectively.

Author Contributions: This work was carried out in collaboration among all authors. Z.L. investigated and conceived of the work. S.G. provided supervision and guidance in the theoretical analysis. Z.L. carried out the theoretical analysis and mechanical design. Z.L. carried out the FEM simulations. L.J. validated the calculation and simulation results. Z.L. wrote the paper. L.J. helped Z.L. improve the quality of the work. H.L. and S.N. commented on the work. All authors have read and agreed to the published version of the manuscript.

Funding: This research received no external funding.

Acknowledgments: The authors would like to thank Yanwei Guan for assistance with FEM simulations.

Conflicts of Interest: The authors declare no conflict of interest.

Appendix A

For this analysis the drive/sense beams are divided into three sections: AB, BC and CD. The applied torque M_0 provided by the drive/sense frame on the left side of AB segment will constrain the rotation of the beam from Figure 5. The torques of each section of the elastic beam can be obtained by establishing a local rectangular coordinate system ($\xi - \delta$) for the three sections.

$$\text{AB section}: M_1 = M_0 - F_y \cdot \xi \tag{A1}$$

$$\text{BC section}: M_2 = M_0 - F_y \cdot l_1 + F_x \cdot \xi \tag{A2}$$

$$\text{CD section}: M_3 = M_0 - F_y \cdot (l_3 - \xi) + F_x \cdot l_2 \tag{A3}$$

where ξ is the independent variable of the local coordinate system.

According to elastic mechanics and material mechanics, the strain energy of the entire drive/sense beam can be obtained.

$$U = \int_0^{l_1} \frac{M_1^2}{2EI_1} d\xi + \int_0^{l_2} \frac{M_2^2}{2EI_2} d\xi + \int_0^{l_3} \frac{M_3^2}{2EI_3} d\xi \tag{A4}$$

The elastic stiffness of drive/sense beam in the direction of y-axis will be explored through Castigliano's second theorem, we assume that a force is applied in the y-axis. At this point, the angle and the displacement along the x-axis of the end of the elastic beam (point A) are both 0. We can obtain that:

$$\theta_z = \frac{\partial U}{\partial M_0} = \int_0^{l_1} \frac{M_1}{EI_1} \frac{\partial M_1}{\partial M_0} d\xi + \int_0^{l_2} \frac{M_2}{EI_2} \frac{\partial M_2}{\partial M_0} d\xi + \int_0^{l_3} \frac{M_3}{EI_3} \frac{\partial M_3}{\partial M_0} d\xi = 0 \tag{A5}$$

$$\delta_x = \frac{\partial U}{\partial F_x} = \int_0^{l_1} \frac{M_1}{EI_1} \frac{\partial M_1}{\partial F_x} d\xi + \int_0^{l_2} \frac{M_2}{EI_2} \frac{\partial M_2}{\partial F_x} d\xi + \int_0^{l_3} \frac{M_3}{EI_3} \frac{\partial M_3}{\partial F_x} d\xi = 0 \tag{A6}$$

Substituting Equation (A1), (A2) and (A3) into Equations (A5), we obtain:

$$M_0 = AF_x + BF_y \tag{A7}$$

where

$$A = -\frac{I_1 l_2 (2I_2 l_3 + l_2 I_3)}{2(I_1 I_2 l_3 + I_1 l_2 I_3 + l_1 I_2 I_3)},\ B = \frac{I_1 I_2 l_3 (2l_1 - l_3) + l_1 I_3 (2I_1 l_2 + l_1 I_2)}{2(I_1 I_2 l_3 + I_1 l_2 I_3 + l_1 I_2 I_3)} \tag{A8}$$

Substituting Equation (A7) into Equations (A1), (A2) and (A3), we obtain:

$$\begin{cases} M_1 = AF_x + (B - \xi)F_y \\ M_2 = (A + \xi)F_x + (B - l_1)F_y \\ M_3 = (A + l_2)F_x + (B - l_3 + \xi) \cdot F_y \end{cases} \tag{A9}$$

Substituting Equation (A9) into Equations (A6), we obtain:

$$F_x = CF_y \tag{A10}$$

where

$$C = -\frac{I_1 I_2 l_3 (A + l_2)(B - l_1 + l_3/2) + I_1 l_2 I_3 (A + l_2/2)(B - l_1) + l_1 I_2 I_3 A (B - l_1/2)}{I_1 I_2 l_3 (A + l_2)^2 + I_1 l_2 I_3 \left(A^2 + l_2 A + l_2^2/3\right) + l_1 I_2 I_3 A^2} \tag{A11}$$

Substituting Equation (A10) into Equations (A9), we obtain:

$$\begin{cases} M_1 = (AC + B - \xi)F_y \\ M_2 = (AC + C\xi + B - l_1)F_y \\ M_3 = (AC + Cl_2 + B - l_3 + \xi)F_y \end{cases} \tag{A12}$$

The Castigliano's second theorem is used to calculate the displacement in the direction of *y*-axis at point A.

$$\delta_y = \frac{\partial U}{\partial F_y} = \int_0^{l_1} \frac{M_1}{EI_1} \frac{\partial M_1}{\partial F_y} d\xi + \int_0^{l_2} \frac{M_2}{EI_2} \frac{\partial M_2}{\partial F_y} d\xi + \int_0^{l_3} \frac{M_3}{EI_3} \frac{\partial M_3}{\partial F_y} d\xi \tag{A13}$$

Substitute Equation (A12) into Equation (A13) and simplify it, we can obtain that:

$$\delta_y = \frac{F_y D}{E} \tag{A14}$$

where

$$D = \frac{\begin{pmatrix} I_1I_2l_3\Big((A+l_2)^2C^2+(A+l_2)(2B-2l_1+l_3)C+l_1^2-(2B+l_3)l_1+l_3^2/3+l_3B+B^2\Big)+ \\ I_1l_2I_3\Big(\Big(A^2+l_2A+l_2^2/3\Big)C^2+C(2A+l_2)(B-l_1)+(B-l_1)^2\Big)+l_1I_2I_3\Big(A^2C^2+AC(2B-l_1)+B^2-l_1B+l_1^2/3\Big)\end{pmatrix}}{I_1I_2I_3} \quad \text{(A15)}$$

The elastic stiffness of drive/sense beam in the direction of y-axis can be obtained.

$$K_{dsy} = \frac{E}{D} \quad \text{(A16)}$$

The same method is used to derive the elastic stiffness of drive/sense beam in the direction of x-axis.

$$K_{dsx} = \frac{E}{H} \quad \text{(A17)}$$

where

$$H = \frac{\begin{pmatrix} I_1I_2l_3\Big(\Big(l_1^2-(2B+l_3)l_1+l_3^2/3+Bl_3+B^2\Big)G^2+(A+l_2)(2B-2l_1+l_3)G+(A+l_2)^2\Big)+ \\ I_1l_2I_3\Big((B-l_1)^2G^2+(2A+l_2)(B-l_1)G+\Big(A^2+Al_2+l_2^2/3\Big)\Big)+l_1I_2I_3\Big(\Big(B^2-Bl_1+l_1^2/3\Big)G^2+AG(2B-l_1)+A^2\Big)\end{pmatrix}}{I_1I_2I_3} \quad \text{(A18)}$$

$$G = -\frac{I_1I_2l_3(A+l_2)(B-l_1+l_3/2)+I_1l_2I_3(A+l_2/2)(B-l_1)+l_1I_2I_3A(B-l_1/2)}{I_1I_2l_3\Big(l_1^2-(2B+l_3)l_1+B^2+Bl_3+l_3^2/3\Big)+I_1l_2I_3(B-l_1)^2+l_1I_2I_3\Big(B^2-Bl_1+l_1^2/3\Big)} \quad \text{(A19)}$$

References

1. Shkel, A.M. Type I and type II micromachined vibratory gyroscopes. In Proceedings of the IEEE/ION Position, Location, and Navigation Symposium, Coronado, CA, USA, 24–27 April 2006; ION: Coronado, CA, USA, 2006; pp. 586–593.
2. Xia, D.; Yu, C.; Kong, L. The development of micromachined gyroscope structure and circuitry technology. *Sensors* **2014**, *14*, 1394–1473. [CrossRef] [PubMed]
3. Efimovskaya, A.; Lin, Y.-W.; Shkel, A.M. Origami-like 3-D folded MEMS approach for miniature inertial measurement unit. *J. Microelectromech. Syst.* **2017**, *26*, 1030–1039. [CrossRef]
4. Putty, M.W. A micromachined vibrating ring gyroscope. Doctoral Dissertation, University of Michigan, Ann Arbor, MI, USA, 1995.
5. Ayazi, F.; Najafi, K. A HARPSS polysilicon vibrating ring gyroscope. *J. Microelectromech. Syst.* **2001**, *10*, 169–179. [CrossRef]
6. Chang, C.O.; Chang, G.E.; Chou, C.S.; Chang Chien, W.T.; Chen, P.C. In-plane free vibration of a single-crystal silicon ring. *Int. J. Solids Struct.* **2008**, *45*, 6114–6132. [CrossRef]
7. Wang, J.; Chen, L.; Zhang, M.; Chen, D. A micro-machined vibrating ring gyroscope with highly symmetric structure for harsh environment. In Proceedings of the 2010 5th IEEE International Conference on Nano/Micro Engineered and Molecular Systems, Xiamen, China, 20–23 January 2010.
8. Yoon, S.W.; Lee, S.; Najafi, K. Vibration sensitivity analysis of MEMS vibratory ring gyroscopes. *Sens. Actuators A Phys.* **2011**, *171*, 163–177. [CrossRef]
9. Yoon, S.; Park, U.; Rhim, J.; Yang, S.S. Tactical grade MEMS vibrating ring gyroscope with high shock reliability. *Microelectron. Eng.* **2015**, *142*, 22–29. [CrossRef]
10. Zaman, M.F.; Sharma, A.; Amini, B.V.; Ayazi, F. The resonating star gyroscope. In Proceedings of the IEEE International Conference on Micro Electro Mechanical Systems, Miami Beach, FL, USA, 30 January–3 February 2005.
11. Zaman, M.F.; Sharma, A.; Ayazi, F. The resonating star gyroscope: A novel multiple-shell silicon gyroscope with sub-5 deg/hr Allan deviation bias instability. *IEEE Sens. J.* **2009**, *9*, 616–624. [CrossRef]
12. Chen, L.; Chen, D.; Wang, J. The design and analysis of a robust micro-machined vibrating ring gyroscope. In Proceedings of the 2008 International Conference on Optical Instruments and Technology: MEMS/NEMS Technology and Applications, Beijing, China, 16–19 November 2008.

13. Chen, D.; Zhang, M.; Wang, J. An electrostatically actuated micromachined vibrating ring gyroscope with highly symmetric support beams. In Proceedings of the IEEE SENSORS 2010 Conference, Waikoloa, HI, USA, 1–4 November 2010.
14. Tao, Y.; Wu, X.; Xiao, D.; Wu, Y.; Cui, H.; Xi, X.; Zhu, B. Design, analysis and experiment of a novel ring vibratory gyroscope. *Sens. Actuators A Phys.* **2011**, *168*, 286–299. [CrossRef]
15. Cao, H.; Liu, Y.; Kou, Z.; Zhang, Y.; Shao, X.; Gao, J.; Huang, K.; Shi, Y.; Tang, J.; Shen, C.; et al. Design, fabrication and experiment of double U-beam MEMS vibration ring gyroscope. *Micromachines* **2019**, *10*, 186. [CrossRef]
16. Chikovani, V.V.; Tsiruk, H.V. Shock resistance of differential type ring-like resonator vibratory gyroscope. *Electron. Control. Syst.* **2014**, *4*, 79–83. [CrossRef]
17. Hu, Z.X.; Gallacher, B.J.; Burdess, J.S.; Fell, C.P.; Townsend, K. A parametrically amplified MEMS rate gyroscope. *Sens. Actuators A Phys.* **2011**, *167*, 249–260. [CrossRef]
18. Nitzan, S.H.; Zega, V.; Li, M.; Ahn, C.H.; Corigliano, A.; Kenny, T.W.; Horsley, D.A. Self-induced parametric amplification arising from nonlinear elastic coupling in a micromechanical resonating disk gyroscope. *Sci. Rep.* **2015**, *5*, 9036. [CrossRef] [PubMed]
19. Polunin, P.M.; Shaw, S.W. Self-induced parametric amplification in ring resonating gyroscopes. *Int. J. Non-Linear Mech.* **2017**, *94*, 300–308. [CrossRef]
20. Gallacher, B.J.; Hedley, J.; Burdess, J.S.; Harris, A.J.; Rickard, A.; King, D.O. Electrostatic tuning of a micro-ring gyroscope. In Proceedings of the Technical Proceedings 2004 NSTI Nanotechnology Conference and Trade Show, Boston, MA, USA, 7–11 March 2004; pp. 430–433.
21. Gallacher, B.J.; Hedley, J.; Burdess, J.S.; Harris, A.J.; Rickard, A.; King, D.O. Electrostatic correction of structural imperfections present in a microring gyroscope. *J. Microelectromech. Syst.* **2005**, *14*, 221–234. [CrossRef]
22. Hu, Z.X.; Gallacher, B.J.; Burdess, J.S.; Bowles, S.R.; Grigg, H.T.D. A systematic approach for precision electrostatic mode tuning of a MEMS gyroscope. *J. Micromech. Microeng.* **2014**, *24*, 125003. [CrossRef]
23. Martynenko, Y.G.; Merkuryev, I.V.; Podalkov, V.V. Control of nonlinear vibrations of vibrating ring microgyroscope. *Mech. Solids* **2008**, *43*, 379–390. [CrossRef]
24. El-Sayed, A.M.; Ghoneima, M.; Mahmoud, M.A.E. Modeling of nonlinearities in vibratory ring gyroscopes. In Proceedings of the 2013 Second International Japan-Egypt Conference on Electronics, Communications and Computers (JEC-ECC), Cairo, Egypt, 17–19 December 2013.
25. Chouvion, B.; McWilliam, S.; Popov, A.A. Effect of nonlinear electrostatic forces on the dynamic behaviour of a capacitive ring-based Coriolis vibrating gyroscope under severe shock. *Mech. Syst. Signal Process.* **2018**, *106*, 395–412. [CrossRef]
26. Liang, D.D.; Yang, X.D.; Zhang, W.; Ren, Y.; Yang, T.Z. Linear, nonlinear dynamics, and sensitivity analysis of a vibratory ring gyroscope. *Theor. Appl. Mech. Lett.* **2018**, *8*, 393–403. [CrossRef]
27. Maslov, A.A.; Maslov, D.A.; Merkuryev, I.V.; Podalkov, V.V. Dynamics of the ring micromechanical gyroscope taking into account the nonlinear stiffness of the suspension. In Proceedings of the 2019 26th Saint Petersburg International Conference on Integrated Navigation Systems (ICINS), Saint Petersburg, Russia, 27–29 May 2019.
28. Sieberer, S.; McWilliam, S.; Popov, A.A. Nonlinear electrostatic effects in MEMS ring-based rate sensors under shock excitation. *Int. J. Mech. Sci.* **2019**, *157*, 485–497. [CrossRef]
29. Trusov, A.A.; Schofield, A.R.; Shkel, A.M. Micromachined rate gyroscope architecture with ultra-high quality factor and improved mode ordering. *Sens. Actuators A Phys.* **2011**, *165*, 26–34. [CrossRef]
30. Guan, Y.; Gao, S.; Jin, L.; Cao, L. Design and vibration sensitivity of a MEMS tuning fork gyroscope with anchored coupling mechanism. *Microsyst. Technol.* **2015**, *22*, 247–254. [CrossRef]
31. Guan, Y.; Gao, S.; Liu, H.; Jin, L.; Niu, S. Design and vibration sensitivity analysis of a MEMS tuning fork gyroscope with an anchored diamond coupling mechanism. *Sensors* **2016**, *16*, 468. [CrossRef] [PubMed]
32. Yoon, S.W. Vibration Isolation and Shock Protection for MEMS. Doctoral Dissertation, University of Michigan, Ann Arbor, MI, USA, 2009.
33. Li, Z.; Gao, S.; Jin, L.; Liu, H.; Guan, Y.; Peng, S. Design and mechanical sensitivity analysis of a MEMS tuning fork gyroscope with an anchored leverage mechanism. *Sensors* **2019**, *19*, 3455. [CrossRef] [PubMed]
34. Fan, K.; Che, L.; Xiong, B.; Wang, Y. A silicon micromachined high-shock accelerometer with a bonded hinge structure. *J. Micromech. Microeng.* **2007**, *17*, 1206–1210. [CrossRef]

35. Ren, J.; Liu, C.-Y.; Li, M.-H.; Chen, C.-C.; Chen, C.-Y.; Li, C.-S.; Li, S.-S. A mode-matching 130-kHz ring-coupled gyroscope with 225 ppm initial driving/sensing mode frequency splitting. In Proceedings of the 2015 Transducers—2015 18th International Conference on Solid-State Sensors, Actuators and Microsystems (TRANSDUCERS 2015), Anchorage, AK, USA, 21–25 June 2015.
36. Kim, J.; Cho, D.-I.D.; Muller, R.S. Why is (111) silicon a better mechanical material for MEMS? In *Transducers' 01 Eurosensors XV*; Springer: Berlin/Heidelberg, Germany, 2001; pp. 662–665.
37. Qin, Z.; Gao, Y.; Jia, J.; Ding, X.; Huang, L.; Li, H. The Effect of the Anisotropy of Single Crystal Silicon on the Frequency Split of Vibrating Ring Gyroscopes. *Micromachines* **2019**, *10*, 126. [CrossRef]